drones

MDPI

Article

$\mathcal{L}_1$ Adaptive Control for Small-Scale Unmanned Helicopters: Enhancing Speed Regulation

Giulia Bertolani [1], Andrea Dan Ryals [2], Emanuele Luigi de Angelis [1,*], Lorenzo Pollini [2] and Fabrizio Giulietti [1]

[1] Department of Industrial Engineering, University of Bologna, 47121 Forlí, Italy; giulia.bertolani2@unibo.it (G.B.); fabrizio.giulietti@unibo.it (F.G.)
[2] Department of Information Engineering, University of Pisa, 56017 Pisa, Italy; andrea.ryals@phd.unipi.it (A.D.R.); lorenzo.pollini@unipi.it (L.P.)
* Correspondence: emanuele.deangelis4@unibo.it; Tel.: +39-0543-374-453

Abstract: This paper focuses on the application of $\mathcal{L}_1$ adaptive control to the speed autopilot loop of small-scale unmanned helicopters. The $\mathcal{L}_1$ adaptive control technique is investigated for its potential to provide reliable speed control, particularly in handling external disturbances and model uncertainties. Although $\mathcal{L}_1$ adaptive control has been widely studied, its application to small-scale unmanned helicopters remains relatively unexplored. Through numerical simulations and a preliminary experimental test campaign conducted on a small rotary-wing platform, this paper contributes to validating $\mathcal{L}_1$ adaptive control as a promising solution for speed regulation in unmanned helicopter platforms.

Keywords: unmanned helicopter; guidance, navigation, and control; control system; $\mathcal{L}_1$ adaptive control; drone

check for updates

Citation: Bertolani, G.; Ryals, A.D.; de Angelis, E.L.; Pollini, L.; Giulietti, F. $\mathcal{L}_1$ Adaptive Control for Small-Scale Unmanned Helicopters: Enhancing Speed Regulation. *Drones* **2024**, *8*, 649. https://doi.org/10.3390/drones8110649

Academic Editor: Xiangwei Bu

Received: 2 October 2024
Revised: 30 October 2024
Accepted: 5 November 2024
Published: 6 November 2024

1. Introduction

Unmanned small-scale helicopters have grown in popularity over the last decade due to their versatility in a wide range of mission scenarios and applications such as load transportation, environmental monitoring [1], search and rescue, remote sensing [2], agricultural applications, and surveillance [3]. Indeed, the key feature of rotary-wing unmanned aerial vehicles (UAVs) is the capability to perform hovering flight conditions and near-vertical climb and descent trajectories. Thus, the growing request for agile, efficient, and autonomous unmanned aerial platforms [4,5] makes the design of robust and reliable control algorithms a mandatory task. Currently, the proportional–integral–derivative (PID) architecture is widely used because of its straightforward design process and its performance in a large variety of applications [1]. Nonetheless, since helicopters show an intrinsically unstable behavior and exhibit a strong dynamic coupling, PID controllers may not represent the best option to guarantee required closed-loop performance, especially in the case of modeling uncertainties and/or aggressive maneuvers, where PID controllers struggle with suppressing coupling effects between the longitudinal, lateral, and directional axes.

UAV advance control techniques include H_∞ structures, which are well known for their inherent robustness against uncertainties and disturbances [6,7] but may lead to undesired performance degradation. Backstepping control is a nonlinear technique widely used for various UAVs [8–10]. Improved tracking performance, robustness to uncertainty, and effective handling of nonlinearities are benefits of this method. Backstepping control also shows some limitations due to the complexity of the design process, which may require a deep understanding of the system dynamics and the tuning of several parameters. Sliding mode control (SMC) has been effectively used in nonlinear under-actuated systems due to its insensitivity to parameter changes and disturbances [11,12]. However, the main drawback is the chattering phenomena, a characteristic oscillation at the switching surface,

leading to increased wear and tear on actuators. Feedback linearization involves converting the complex nonlinear dynamics of the helicopter into a linear system by making certain changes in the coordinates of the system and designing appropriate control laws [8,13–15]. Any inaccuracies or uncertainties in the model can result in performance degradation or instability. The incremental nonlinear dynamic inversion (INDI) control approach is a sensor-based methodology designed to enhance robustness by minimizing reliance on intricate models. Unlike traditional control methods, INDI strategically incorporates sensor feedback to adapt and respond to dynamic changes in the system, thereby making it more resilient in the face of uncertainties. Nevertheless, the efficacy of the INDI controller is intrinsically tied to the precision of onboard measurements and the impact of actuator delays. On the other hand, actuator delays introduce a temporal lag between the control command and the system's response, posing a challenge for real-time control and stability. Some recent papers address the implementation of INDI control to helicopters with satisfactory results [16,17]. Model predictive control (MPC) is a powerful technique that can be effectively applied in the field of helicopter control [18–20]. Essentially, MPC uses a system model to predict the future outputs and states of a controlled system while also optimizing control inputs to minimize a given cost function. The effectiveness depends on the model's accuracy for predictions. To reduce model dependency, adaptive model predictive control has been proposed for simple systems [21,22]. Adaptive control techniques continuously adjust the control parameters based on real-time system information and are well suited for helicopters because of their nonlinear dynamics and uncertainties in the models. There is still interest in helicopter control for classical adaptive control systems such as model reference control (MRAC). This technique uses a reference model that represents the desired dynamic performance of the system. The computation of an adaptive control input is determined by the discrepancy between the attained and desired performance. Model uncertainties and disturbances are compensated by the adaptive control input. In the literature, there are some interesting papers on the use of MRAC applied to helicopters [23–27]. The main drawback of MRAC is that an adaptive loop may induce undesired oscillations on the helicopter if adaptation gains are high. High gains mean faster adaptation and improved tracking performance. Thus, methods for achieving large adaptive gain while filtering undesired oscillations are important for adaptive control issues in UAV helicopters.

The $\mathcal{L}_1$ adaptive control ($\mathcal{L}_1$AC) is particularly noted for its ability to separate robustness from quick adaptation while avoiding potential unwanted oscillations. This control theory was pioneered by Hovakimyan and Cao [28–32]. This technique has been successfully applied in the aerospace field. For instance, Wang et al. [33] utilized the $\mathcal{L}_1$ adaptive control with a neural network-based predictor for autonomous aerial refueling. Gregory et al. [34] developed an $\mathcal{L}_1$ control system for fixed-wing aircraft to address both matched and unmatched uncertainties, tested under failure conditions and in highly nonlinear coupled dynamics. Hellmundt et al. [35] applied the $\mathcal{L}_1$ adaptive control to manage uncertainties in fighter aircraft, enhancing system performance. For rotary-wing aircraft, Bichlmeier et al. [36] and Song et al. [37] used piecewise constant adaptation laws for attitude rate control and vertical flight, respectively. Guerreiro et al. [38] achieved the state space stabilization of speed for an autonomous small-scale helicopter with an $\mathcal{L}_1$ adaptive controller. More recently, the same authors developed an $\mathcal{L}_1$ adaptive control system to improve the performance and robustness of a PID attitude controller for an unmanned small-scale helicopter [39].

This paper extends a previous work of the same authors [40] on an $\mathcal{L}_1$ adaptive speed control system designed to maintain optimal performance along a range of different flight conditions and in the presence of wind disturbances.

The main contributions of this paper can be summarized as follows: (1) the development of an adaptive $\mathcal{L}_1$ output feedback controller for the speed controller of a small-scale UAV helicopter; (2) the analysis of control system performance, based on numerical simulations with a comparison with a PI speed controller; and (3) the extension of existing

research presenting experimental flight tests involving $\mathcal{L}_1$ adaptive controls on a remotely piloted helicopter platform. In the literature, to the best of the authors' knowledge, only one other paper displays flight data collected using this controller technique on a small-scale helicopter [41]. Harada et al. [41] presented the experimental application of the $\mathcal{L}_1$ adaptive control to a coaxial rotor micro aerial vehicle (MAV), conducted in an indoor environment. Micro aerial vehicles (MAVs) differ significantly from small-scale unmanned helicopters regarding weight class, with MAVs typically belonging to a much lighter category.

The $\mathcal{L}_1$ adaptive control architecture tested in this paper has demonstrated improved tracking and rejection capabilities in a simulated environment. Simulations allow for the reproduction of consistent atmospheric and reference conditions across experiments, effectively highlighting the enhanced performance. In future research, the authors aim to comprehensively test both PI and adaptive solutions, gathering more data to substantiate their findings. This paper primarily outlines the preliminary experimental results achieved and contributes additional experimental data to the existing literature on the $\mathcal{L}_1$ adaptive control for small-scale helicopters.

The paper is organized as follows: Section 2 describes the control systems architecture; Section 3 introduces the UAV mathematical model used for simulations; Section 4 presents the simulation results; Section 5 gives an overview of the experimental setup for the flight test and presents experimental results; finally, Section 6 provides concluding remarks.

2. Control System Architecture

Two primary control loops comprise the structure of the helicopter control system, as depicted in Figure 1. PID controllers provide the basis of the attitude's inner control loop, together with heading hold and altitude hold controllers. The $\mathcal{L}_1$ adaptive control handles the external speed control loop, and its implementation is detailed in Section 2.3.

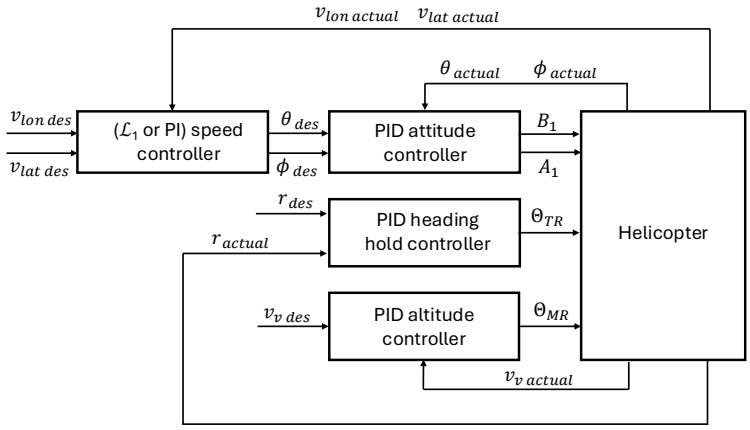

Figure 1. Helicopter control system architecture.

2.1. PID Attitude Controllers

The PID approach is the basis for the inner control loop on the attitude of the UAV helicopter on both of the two independent axes, roll and pitch. It consists of a cascade control system [42]. The principal controller in the outer loop assesses the inner loop's set point using its dynamic. For stability to be improved, this dynamic should be significantly quicker than the outer loop. As for the $\mathcal{L}_1$ speed controller implementation given in Section 2.3, since longitudinal and lateral attitude control is the same, only the longitudinal one is briefly described. The attitude control is achieved with an inner loop on the angular rate q in a proportional–integral (PI) scheme, while the outer loop concerns the angle θ with a proportional (P) gain.

The error signals are defined as follows:

$$\begin{cases} \epsilon_\theta = \theta_{des} - \theta_{act} \\ \epsilon_q = q_{des} - q_{act} \end{cases} \tag{1}$$

The cascade P-PI control output result is the following:

$$\begin{cases} q_{des} = K_{P\theta}\epsilon_\theta \\ B_1 = K_{Pq}\epsilon_q + K_{Iq}\int_0^t \epsilon_q dt \end{cases} \tag{2}$$

where K_P is the proportional gain, K_I is the integral one, and B_1 is the longitudinal cyclic command.

2.2. PID Heading Hold and Altitude Hold Controllers

The PID control method is a technique involving both heading hold and altitude hold controllers, which have a structure similar to the cascade attitude hold controllers. The input signal is where attitude hold controllers differ in longitudinal and lateral attitude axes. As a matter of fact, the yaw rate r, not the yaw angle ψ, is the input signal for the heading hold controller. The integration of the error signal on the yaw rate ϵ_r yields the required yaw angle of the outer loop. The error signals are defined as follows:

$$\begin{cases} \epsilon_\psi = \int_0^t \epsilon_r dt \\ \epsilon_r = r_{des} - r_{act} \end{cases} \tag{3}$$

The cascade control output results are as follows:

$$\begin{cases} r_{des} = K_{P\psi}\epsilon_\psi \\ \Theta_{TR} = K_{Pr}\epsilon_r + K_{Ir}\int_0^t \epsilon_r dt \end{cases} \tag{4}$$

Control is exercised over the vertical speed and acceleration on the main rotor collective. Like the heading hold controller, the reference vertical velocity is integrated to have a reference command signal. The derivative action on the vertical acceleration is the primary distinction from the other PID controllers that have been shown. The error signals are defined as follows:

$$\begin{cases} \epsilon_z = \int_0^t v_v dt \\ \epsilon_v = v_{v\ des} - v_{v\ act} \end{cases} \tag{5}$$

The control output results are as follows:

$$\begin{cases} v_{v\ des} = K_{Pz}\epsilon_z \\ \Theta_{MR} = K_{Pv_v}\epsilon_{v_v} + K_{Iv_v}\int_0^t \epsilon_{\dot{z}} dt + K_{Da_v}a_v \end{cases} \tag{6}$$

2.3. $\mathcal{L}_1$ Adaptive Speed Hold Controllers

The complete theory of $\mathcal{L}_1$AC can be found in [28–30,32,41]. We assume that the system can be described by the following model:

$$y = G_p(s)(u + d) \tag{7}$$

where G_p is the plant transfer function, y is the system output, u is the control input, and d lumps the uncertainties affecting the system. It is assumed that $d(t) = f(t, y(t))$ is the Lipschitz function with constant L [28–30].

The so-called predictor is then described by the following transfer function:

$$\hat{y} = G_m(s)(u + \hat{\sigma}) \tag{8}$$

The ideal σ that makes Equation (7) behave like the predictor transfer function in Equation (8) is as follows:

$$\sigma(s) = \frac{\big(G_p(s) - G_m(s)\big)u(s) + G_p(s)d(s)}{G_m(s)} \tag{9}$$

In order to estimate the value of σ, the following adaptive law can be used:

$$\dot{\hat{\sigma}}(s) = \Gamma \text{proj}(\hat{\sigma}, -\tilde{y}) \tag{10}$$

where proj() is the projection operator as presented in [43], and $\tilde{y} = \hat{y} - y$ is the error between the predictor and the measured output.

The adaptive input to the system is chosen as follows:

$$u_{\mathcal{L}_1} = C(s)(Kr - \hat{\sigma}) \tag{11}$$

where $C(s)$ is a unitary gain low-pass filter. To have a stable adaptive loop, the filter has to be chosen in order to satisfy the following conditions:

$$\|G(s)\|_{\mathcal{L}_1} L < 1 \tag{12}$$

where $\|\|_{\mathcal{L}_1}$ is the $\mathcal{L}_1$ norm as presented in [31]. $G(s)$ is defined as follows:

$$G(s) = H(s)(1 - C(s)) \tag{13}$$

and $H(s)$ is as follows:

$$H(s) = \frac{G_p(s)G_m(s)}{C(s)G_p(s) + (1 - C(s))G_m(s)} \tag{14}$$

In this work, the adaptive speed control implementation on both axes is identical. Therefore, the implementation will be described only once for the longitudinal axis, considering that the same structure is also applied on the lateral axis. The longitudinal and lateral speed feedback loops are designed on the principle that the helicopter's velocities along these axes are directly influenced by the fuselage's pitch and roll tilts [44]. Adjusting the pitch angle induces velocity along the longitudinal axis while adjusting the roll angle induces velocity along the lateral axis. The desired dynamic responses between pitch and longitudinal speed and roll and lateral speed are then determined using a second-order model, defined by specific damping (ξ_{lon} and ξ_{lat}) and natural frequency (ω_{lon} and ω_{lat}) characteristics.

The selected reference model is a second-order reference model as follows:

$$G_{lon}(s) = K_\theta \frac{\omega_{lon}^2}{s^2 + 2\xi_{lon}\omega_{lon}s + \omega_{lon}^2} \tag{15}$$

$$\hat{v}_{lon} = G_{lon}(s)\theta \tag{16}$$

where K_θ is the longitudinal transfer function gain, $\hat{v}_{lon}$ is the helicopter longitudinal speed of the reference model in a local vertical axes frame (described in Section 3), and θ is the pitch attitude angle of the UAV helicopter.

The low-pass filter is a second-order unitary gain transfer function as follows:

$$C_{lon}(s) = \frac{\omega_f^2}{s^2 + 2\xi_f\omega_f s + \omega_f^2} \tag{17}$$

where ξ_f and ω_f are the damping and natural frequencies of the low-pass filter.

The adaptive input can be written as follows:

$$u_{\mathcal{L}_1} = C_{lon}(s)(K_{lon}v_{lon,r} - \sigma_{lon}) \tag{18}$$

where K_{lon} is feedforward gain, $v_{lon,r}$ is the reference longitudinal speed, and σ_{vlon} values are the adaptive parameters estimated by means of the following adaptive control laws:

$$\dot{\sigma}_{lon} = \Gamma \text{proj}(\sigma_{lon}, -e_{lon}) \tag{19}$$

Here, $e_{lon} = \hat{v}_{lon} - v_{lon}$ represents the error between the reference model and the actual longitudinal velocity of the helicopter. This error quantifies the discrepancy between the desired longitudinal response and the helicopter's actual behavior along the longitudinal axis. To achieve the desired dynamic response described by the reference model, the adaptive controller must compensate for this error, ensuring that the system closely follows the intended model behavior. The design parameters of the $\mathcal{L}_1$ adaptive longitudinal and lateral controllers are given in Table 1.

Table 1. $\mathcal{L}_1$ longitudinal and lateral speed controller parameters.

Control Parameters	Values	Units
Γ	10,000	
ω_f	2	rad/s
$\xi_f = \xi_f$	1	
$\omega_{lon} = \omega_{lat}$	40	rad/s
$\xi_{lon} = \xi_{lat}$	1	
K_{lon} ine K_{lat}	0.18 0.26	

3. Helicopter Mathematical Model

This section summarizes the mathematical model of the small-scale UAV helicopter utilized for simulations, whose data are reported in Table A1. The data are those of the UAV helicopter SAB Goblin Thunder 700 (SABitaly, Pascoli, Italy), depicted in Figure 2. This model is a nonlinear representation of the dynamic and aerodynamic properties of small-scale unmanned helicopters.

Figure 2. SAB Goblin Black Thunder 700 helicopter.

The mathematical model presented in this paper was mostly derived from the works of Talbot [45] and Heffley [46], which present mathematical modeling of full-scale helicopters. The components of the UAV helicopter that were modeled only include the main rotor, the tail rotor, and the fuselage. The vertical and horizontal tail planes are not included in this model because the small-scale helicopter used for testing does not have them. The main rotor model is based on Talbot's work [45], but the main differences are found in the rotor inflow equations since Pitt–Peters equations have been introduced [47]. The fuselage model is not represented by Talbot equations, but it is modeled as in Heffley's work [46]. The forces and moments that are applied at the center of gravity are the totals of the contributions from all the components of the helicopter plus the forces of gravity. The six-degrees-of-freedom model is derived under the following assumptions:

1. The earth is flat and fixed;
2. Mass, inertia, and center of gravity position are constant, and the vehicle presents a longitudinal plane of symmetry;
3. Gravity acceleration is considered independent of height and hence constant.

The following right-handed orthogonal reference frames were considered (see Figure 3): Let $\mathbb{F}_E = \{O; \mathbf{x}_E, \mathbf{y}_E, \mathbf{z}_E\}$ be the north–east–down (NED) frame; $\mathbb{F}_{hw} = \{H; \mathbf{x}_{hw}, \mathbf{y}_{hw}, \mathbf{z}_{hw}\}$ be the hub-wind frame, whose origin is in the helicopter hub; $\mathbb{F}_{hb} = \{H; \mathbf{x}_{hb}, \mathbf{y}_{hb}, \mathbf{z}_{hb}\}$ is the hub-body frame, which coincides with the hub-wind frame when the system sideslip β_s is zero; $\mathbb{F}_b = \{CG; \mathbf{x}_b, \mathbf{y}_b, \mathbf{z}_b\}$ is the body frame; and the local vertical–local horizontal frame is $\mathbb{F}_{LV} = \{CG; \mathbf{x}_{LV}, \mathbf{y}_{LV}, \mathbf{z}_{LV}\}$, whose origin is in the vehicle CG, and the axes are parallel to $\mathbb{F}_E$, except for an elementary rotation about $\mathbf{z}_E$ of amplitude ψ.

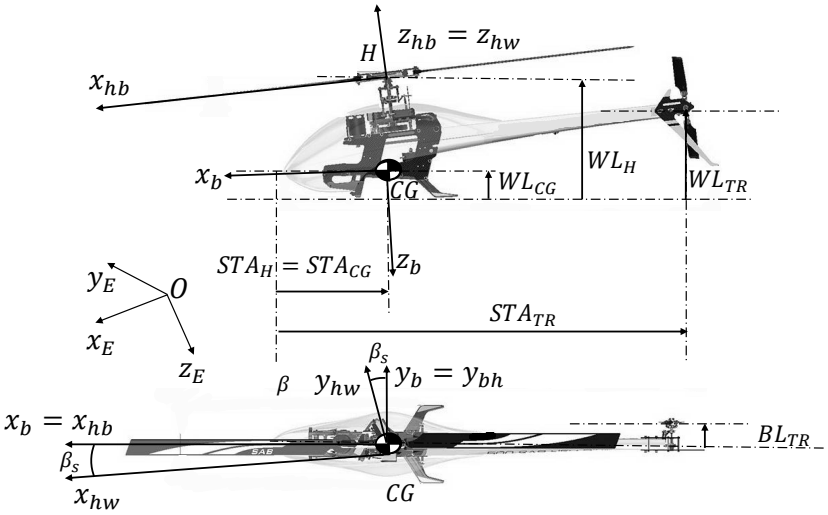

Figure 3. UAV helicopter relevant frames.

In Figure 3, in addition to the reference frames, the distances of the center of gravity, the main rotor, and the tail rotor are also indicated in terms of stationline (STA), waterline (WL), and buttline (BL). Stationlines are measured from the nose of the helicopter along its longitudinal axis, waterlines from the lower part of the skid along the vertical axis, and buttlines from the longitudinal axis of symmetry along the $\mathbf{y}_b$ axis direction. MR denotes the main rotor, TR indicates the tail rotor, and CG represents the center of gravity. These indications are needed to compute the arms in moments calculation, as detailed in Ref. [45].

The Newton–Euler equations of motion projected in the body frame $\mathbb{F}_b$ describe the dynamics of the vehicle that are as follows:

$$\frac{d\boldsymbol{V}}{dt} = -\boldsymbol{\Omega} \times \boldsymbol{V} + \boldsymbol{F}^{(e)}/m \tag{20}$$

$$\frac{d\boldsymbol{\Omega}}{dt} = \boldsymbol{I}^{-1}[-\boldsymbol{\Omega} \times (\boldsymbol{I}\boldsymbol{\Omega}) + \boldsymbol{M}^{(e)}] \tag{21}$$

where $\boldsymbol{\Omega}$ is the angular velocity vector, $\mathbf{V}$ is the linear body velocity vector, $\boldsymbol{F}^{(e)}$ and $\boldsymbol{M}^{(e)}$ are the external forces and moments vectors, $\boldsymbol{J}$ is the inertia tensor about CG with respect to $\mathcal{F}_B$, and m is the total mass of the UAV. While the total moment vector just contains aerodynamic action $\boldsymbol{M}^{(a)}$, the external force vector includes contributions from gravity $\boldsymbol{F}^{(g)}$ and aerodynamic $\boldsymbol{F}^{(a)}$. The vector of gravity force is determined as follows:

$$\boldsymbol{F}^{(g)} = \mathbb{T}_{bE}\begin{bmatrix}0 & 0 & mg\end{bmatrix}^T \tag{22}$$

where $\mathbb{T}_{bE}$ represents the rotation matrix from $\mathbb{F}_E$ to $\mathbb{F}_b$, and g is the gravity constant. The equations for rigid-body kinematics are the following:

$$\begin{bmatrix} \dot{\phi} \\ \dot{\theta} \\ \dot{\psi} \end{bmatrix} = \begin{bmatrix} 1 & \sin\phi\tan\theta & \cos\phi\tan\theta \\ 0 & \cos\phi & -\sin\phi \\ 0 & \sin\phi/\cos\theta & \cos\phi/\cos\theta \end{bmatrix} \boldsymbol{\Omega} \tag{23}$$

$$\frac{d\boldsymbol{X}}{dt} = \mathbb{T}_{bE}^{-1}\mathbf{V} \tag{24}$$

where

$$\mathbb{T}_{bE}^{-1} = \begin{bmatrix} c\theta c\psi & s\phi s\theta c\psi - c\phi s\psi & c\phi s\theta c\psi + s\phi s\psi \\ c\theta s\psi & s\phi s\theta s\psi + c\phi c\psi & c\phi s\theta s\psi - s\phi c\psi \\ -s\theta & s\phi c\theta & c\phi c\theta \end{bmatrix} \tag{25}$$

obtained through a 3–2–1 rotation sequence, where ϕ, θ, and ψ are roll, pitch, and yaw attitude angles, respectively, provided $c(\cdot) = \cos(\cdot)$ and $s(\cdot) = \sin(\cdot)$. $\mathbb{X}_E$ are the position vectors in the $\mathbf{F}_E$ reference frame.

The aerodynamic forces, $\boldsymbol{F}^{(a)} = [F_x, F_y, F_z]^T$, and moments, $\boldsymbol{M}^{(a)} = [M_x, M_y, M_z]^T$, are the sum of the contributions of the helicopter's main rotor, tail rotor and fuselage. The air parameters were calculated from the International Standard Atmosphere (ISA) model as a function of UAV altitude [48].

3.1. Main Rotor Model

Based on [45], the following hypotheses were made:

1. Blade flow stall and compressibility were not taken into account;
2. Rotor blades were rigid in torsion and bending;
3. Linear blade twist;
4. Flapping angles were small, and the simple strip theory was applied [49];
5. Blade flapping was approximated by the first harmonic terms with time-varying coefficients, that is,

$$\beta(t) = a_0 - a_1\cos\xi - b_1\sin\xi \tag{26}$$

where a_0, a_1, b_1 are the coning, longitudinal, and lateral flapping angles, and ξ is blade azimuth.

Different from Talbot's work [45], the mathematical model of the inflow is based on Pitt–Peters [47], where only a constant term is considered that is in $\mathbb{F}_{hw}$

$$\frac{d}{dt}\begin{pmatrix} \lambda_0 \\ \lambda_s \\ \lambda_c \end{pmatrix} = \Omega_h\mathbb{M}^{-1}(-(\mathbb{L}_{nl})^{-1}\begin{pmatrix} \lambda_0 \\ \lambda_s \\ \lambda_c \end{pmatrix} + \boldsymbol{C}_{aero}) \tag{27}$$

with $\lambda_s = \lambda_c = 0$ only taken into account (λ_0). The equations for the vector $\boldsymbol{C}_{aero} = [C_T\&C_L\&C_M]^T$ and the matrices of apparent mass terms $\mathbb{M}$ and of the nonlinear version of the inflow gains $\mathbb{L}_{nl}$ are fully detailed in [47]. The total inflow λ is as follows:

$$\lambda = \frac{w_{hH}}{\Omega_h R_h} - \lambda_0 \tag{28}$$

where w_{hH} is the helicopter vertical velocity component in the hub-wind reference frame, Ω_h is the MR rotational speed, and R_h is the MR radius. The rotor-induced velocity at the disk is calculated using the following formula:

$$v_{hi} = (\frac{w_{hH}}{\Omega_h R_h} - \lambda)\Omega_h R_h \tag{29}$$

Using the momentum theory and analytical integration over the radius, blade forces are calculated based on the aforementioned hypotheses. In Ref. [45], there are detailed

formulas for calculating forces and moments, which are not provided here for the sake of brevity.

3.2. Tail Rotor and Fuselage Model

The tail rotor is modeled in accordance with Ref. [45]. Since the tail rotor flapping frequency is much greater than that of the main rotor system, the tail rotor tip-path plane dynamics are disregarded. Constant state solutions involve moments, flapping angles, and forces. The fuselage is represented as a virtual flat plate drag source with three dimensions [46]. Forces and moments are calculated as a function of the sideslip angle and the angle of attack.

4. Simulation Results

In what follows, the behavior of the $\mathcal{L}_1$ speed controller is shown. The nonlinear model described in Section 3, characterized by the UAV helicopter data listed in Table A1, was utilized for the simulations. It was implemented in a Matlab/Simulink® environment, where differential equations were solved using the Dormand–Prince ode8 method with a frequency of 1000 Hz [50]. In order to test the control system robustness, wind disturbance was added in some of the simulations discussed here. The wind was simulated using three different types of mathematical models. A discrete gust was included on the three axes with an amplitude of $[u_g\ v_g\ w_g] = [3.5\ 3.5\ 3.0]$ m/s, where u_g, v_g and w_g are the gust components. Moreover, a discrete Dryden wind turbulence model was summed to the gust, which is based on the Dryden spectral representation [51]. The wind speed in this instance was set at 15 m/s at a height of 6 m and a direction of 0 degrees clockwise from the north. The third wind model was the shear one, based on what is reported in Ref. [52]. The wind speed was set as in the case of Dryden turbulence.

To assess the performance of the $\mathcal{L}_1$ adaptive controller, the results from a PI speed controller are also given in Section 4.1 and compared in terms of mean errors in Section 4.3. The PI speed controller is a conventional proportional–integral (PI) architecture on both longitudinal and lateral axes, and it is displayed in Figure 1.

The pitch and roll attitude references are computed as follows:

$$\phi_{des} = K_{p,lat} e_{pi,lat} + K_{i,lat} \int_0^t e_{pi,lat} dt \tag{30}$$

$$\theta_{des} = K_{p,lon} e_{pi,lon} + K_{i,lon} \int_0^t e_{pi,lon} dt \tag{31}$$

where $e_{pi,lat} = v_{lat,r} - v_{lat}$ and $e_{pi,lon} = v_{lon,r} - v_{lon}$ are the longitudinal and lateral reference speed tracking errors. $K_{p,lon}$ and $K_{p,lat}$ are the proportional gains and $K_{i,lon}$, and $K_{i,lat}$ are the integral gains of the PI controller.

Its parameters are given in Table 2.

Table 2. PI longitudinal and lateral speed controller parameters.

Control Parameters	Values
$K_{p,lon}$	0.56
$K_{i,lon}$	0.15
$K_{p,lat}$	0.56
$K_{i,lat}$	0.15

Both controllers are asked to follow reference velocities on longitudinal and lateral axes in the local vertical–local horizontal reference frame. The reference signals are as follows:

$$v_{lon} = \begin{cases} v_{M,lon}(0.05\sin(\frac{5}{\pi}t + 0.08) + 0.4\sin(\frac{1}{2\pi}t)) & 0 < t \leq 40 \\ v_{M,lon}(0.05\sin(\frac{5}{\pi}t + 0.08) + 0.2\sin(\frac{1}{2\pi}t)) & t > 40 \end{cases}. \tag{32}$$

where $v_{M,lon} = 10$ m/s is the maximum longitudinal speed, $v_{M,lat} = 7.5$ m/s is the maximum lateral speed, and t is the simulation time.

4.1. PID Speed Control Simulations

In Figure 4, the longitudinal and lateral speed tracking of the PI speed control architecture is shown while flying in calm air. The controller is capable of tracking the reference with satisfactory performance, despite the fact that when a strong front wind is present, this architecture fails to accomplish the speed regulation task, as proven by Figure 5. In this figure, it is clear that the simple PI fails to generate a command capable of both tracking the elaborated reference speed signal and counteracting the wind disturbance action.

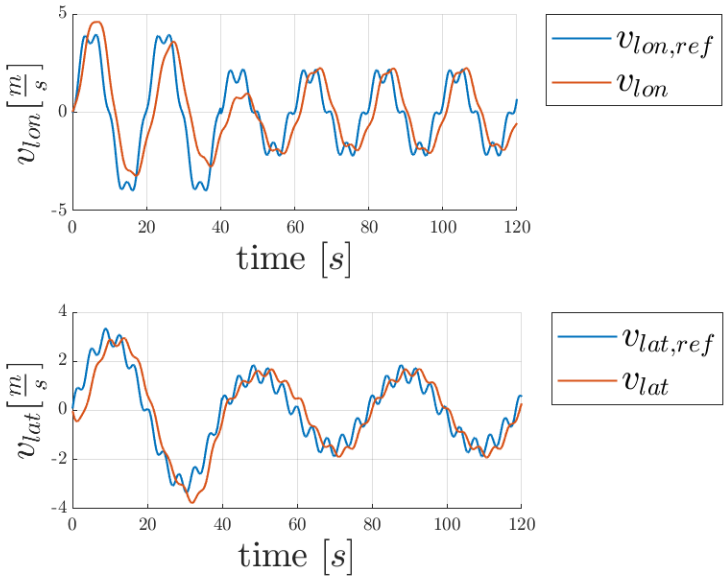

Figure 4. Longitudinal and lateral speed reference tracking in calm air using the PID controller.

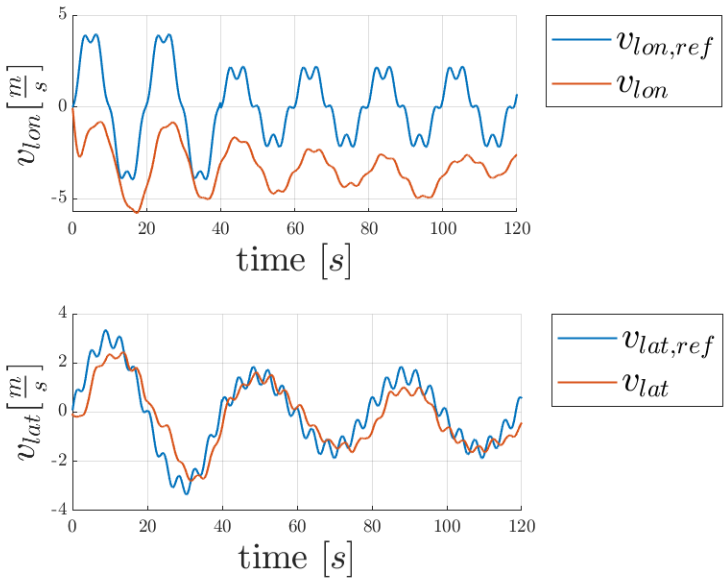

Figure 5. Longitudinal and lateral speed reference tracking in the presence of wind disturbance using the PID controller.

4.2. $\mathcal{L}_1$ Speed Control Simulations

In Figures 6 and 7, the speed tracking results of the $\mathcal{L}_1$ controller in calm air and under the presence of wind disturbances are shown. The tracking in both conditions is satisfactory, and the controller is capable of compensating for the wind disturbances with no noticeable performance degradation.

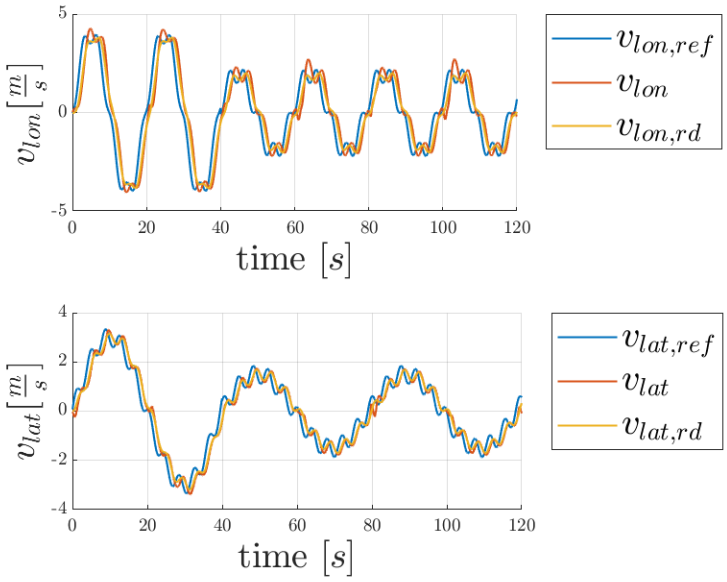

Figure 6. Longitudinal and lateral speed reference tracking in calm air using the $\mathcal{L}_1$ controller.

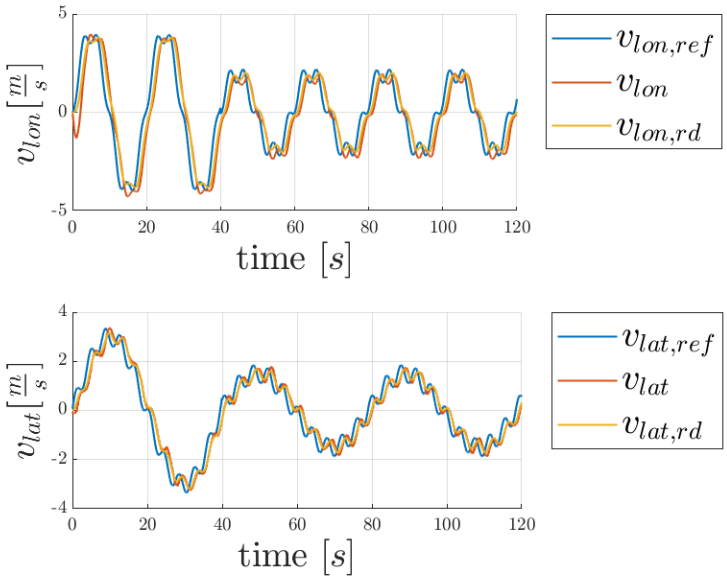

Figure 7. Longitudinal and lateral speed reference tracking in the presence of wind disturbance using the $\mathcal{L}_1$ controller.

4.3. Speed Reference Tracking Performance Assessment

In Figure 8, the normal distributions of longitudinal and lateral reference tracking errors are shown both for the PID controller and for the $\mathcal{L}_1$AC controller when the UAV helicopter is simulated to fly in calm air. In these conditions, both controllers exhibit good tracking capabilities, having almost 0 mean error. The $\mathcal{L}_1$AC shows a less sparse distribution, thus confirming its ability to achieve a better tracking error.

In Figure 9, the normal distributions of longitudinal and lateral reference tracking errors are shown both for the PID controller and the $\mathcal{L}_1$AC controller when the UAV helicopter is simulated to fly under wind disturbances. In these conditions, the $\mathcal{L}_1$AC controller proves to have better tracking performance. The longitudinal speed error distribution for the $\mathcal{L}_1$AC has almost 0 mean error while the PID error tracking distribution not only has a positive mean error but is also more dispersed. Although the later tracking of the two controllers is not that different, the $\mathcal{L}_1$AC has slightly better performance.

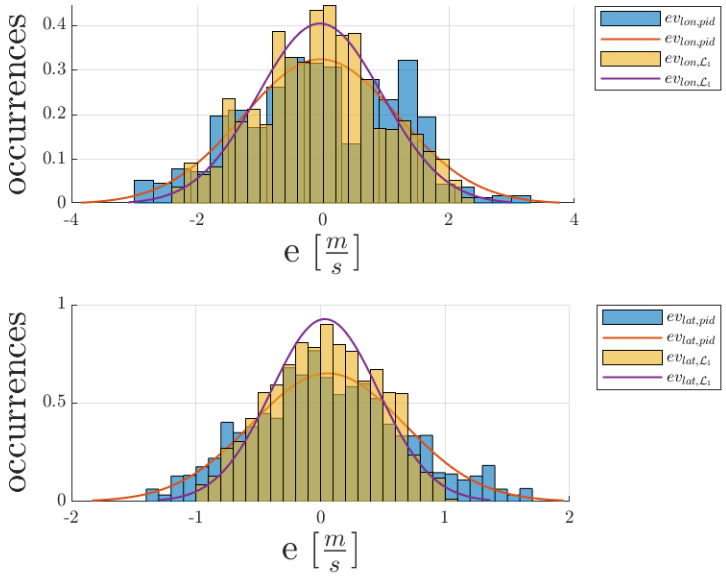

Figure 8. Speed tracking error distribution comparison between $\mathcal{L}_1$ adaptive control and PID control when used in calm air.

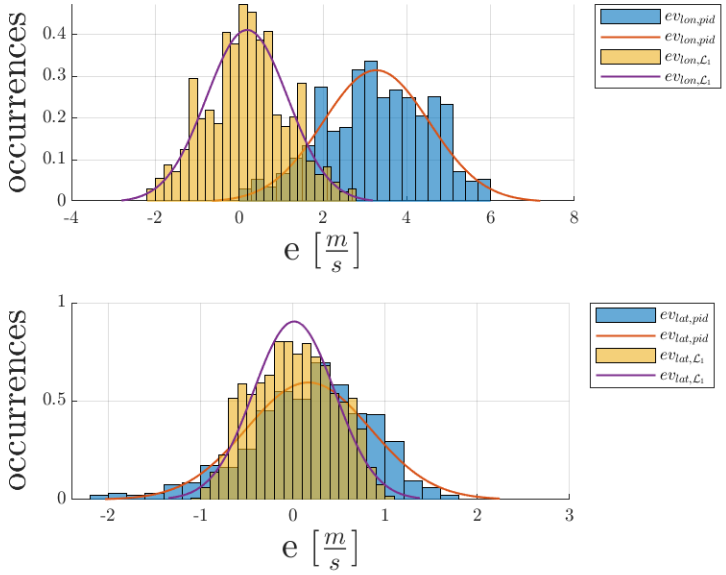

Figure 9. Speed tracking error distribution comparison between $\mathcal{L}_1$ adaptive control and PID control when wind disturbance is present.

5. Experimental Results

5.1. Experimental Test Setup

The experimental setup for this study involved a UAV helicopter equipped with a Pixhawk® Black Cube flight controller (Cubepilot, Australia). The SAB® Goblin Thunder

700 helicopter was used, whose data are reported in Table A1, and the model is shown in Figure 2. This radio commanded (RC) helicopter was equipped with electronic components shown in the scheme of Figure 10.

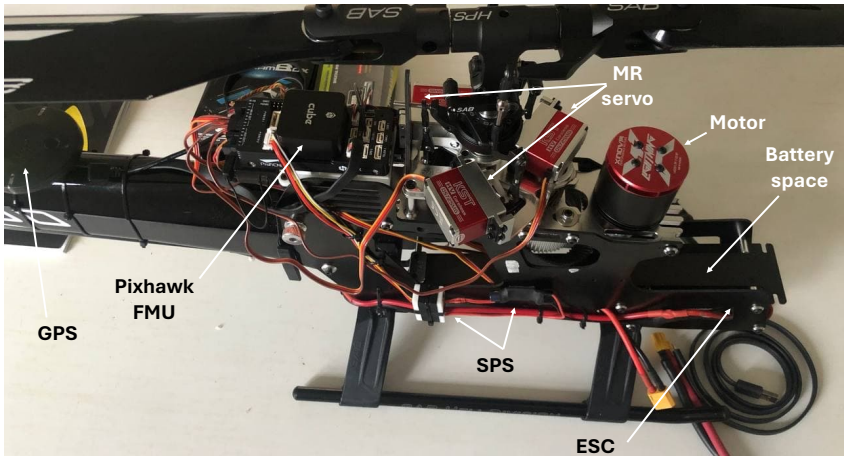

Figure 10. Goblin 700 UAV helicopter electronic components.

The UAV motor was the XNOVA lightning motor 4025-1120KV Shaft A (XNOVA TECHNOLOGY CO), which is a brushless high-performance motor. The power was provided using a Lipo battery with 6 cells, 6300 mAh. As illustrated in the scheme of Figure 10, there was also a safety power switch (SPS), designed for switching off/on the main power supply. The UAV was linked to the radio command (RC) through the related system. In order to govern the electric motor, an electronic speed control (ESC) was employed (Hobbywing Platinum ESC KV 180A, Hobbywing), which was directly connected to the power module and to the autopilot hardware. There were four servo controls KST: three for the main rotor control (collective, roll, and pitch) and one for the tail rotor (yaw axis).

The avionics hardware of the helicopter was a Pixhawk® autopilot (https://pixhawk.org), also indicated as the Pixhawk "flight management unit" (FMU). It included a high-performance microcontroller, based on the Cortex-M4F processor (Arm); an inertial measurement unit (IMU) comprising three-axis gyroscopes and accelerometers; a barometer; and a set of external sensors, including Global Navigation Satellite System (GNSS) and magnetometers. All the important specifications, including data sensors, are reported on the Pixhawk® website [53]. This hardware has the possibility of direct interaction with the Matlab/Simulink® 2023a suite through the toolbox Pixhawk® Pilot Support Package (PSP). By using the PSP, the user can work with Simulink® and directly generate code for the FMU. As a matter of fact, this toolbox automatically translates the Simulink® code into Pixhawk® compatible code languages. Thus, the control software can be directly uploaded on the FMU from Simulink®. In Figure 11, the proposed software architecture is shown. The part of the software uploaded with the Simulink® PSP toolbox on Pixhawk® is highlighted in Figure 11 with orange boxes. This part of the code corresponding to the control system was developed in Matlab/Simulink® and then uploaded on the FMU. The firmware code was generated in Simulink® before being uploaded on the FMU through the PSP UAV Toolbox. It defined the reference and measured signals and provided the helicopter's commands. These were processed with a mixer to generate the proper control signals for servos. The other functionalities such as the interfaces with radio command (RC) inputs, PWM outputs to servos, RPM governor, and sensor data acquisition were managed by the PX4 toolchain. Details on the functionalities of this toolbox can be found on Pixhawk and Matlab/Simulink websites [53,54]. In this figure, the different components of the UAV are illustrated with different colored boxes.

The green box includes the radio command; the light blue box highlights the ESC; the yellow box illustrates the servos, and the purple box shows the motor. The light orange

box contains Pixhawk hardware, while the dark orange box highlights the control system firmware, which was uploaded on the FMU. In the upper part of Figure 11, it is possible to identify the mode switching. This part of the software was used in the UAV helicopter to shift from one flight mode to another. In this software, there are three flight modes: 0, corresponding to a mode in which the pilot inputs are attitude references on the roll, pitch, and yaw axes, as well as the collective manually controlled by the pilot itself; 1 representing the altitude-hold control mode, which is the flight mode 0 with the only difference on collective control, i.e., the pilot commands a desired vertical speed with collective stick input; and 2 corresponding to the $\mathcal{L}_1$ speed control.

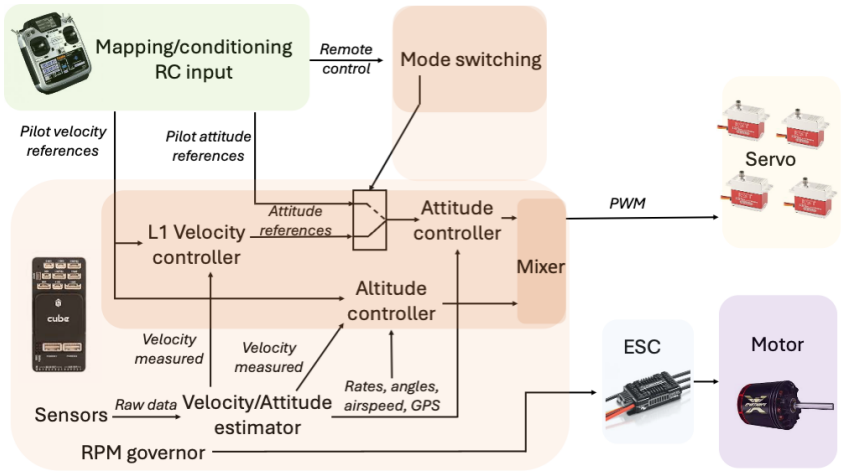

Figure 11. Goblin 700 Flight control architecture.

5.2. Experimental Data Analysis

The proposed adaptive control architecture was tested in flight on the actual UAV helicopter described in Section 5.1. The entire set of control parameters, PID gains, adaptive controller gains, and low-pass filters are given in Tables 1 and 2. The controller gains were initially tuned in a simulation environment before undergoing flight testing. Given the helicopter's complex dynamics, tuning controller gains directly during flight poses significant complexity and safety risks. A primary challenge is developing a mathematical model that produces reliable simulation results, which is essential for ensuring safe and effective initial tuning before flight testing.

The results presented in this section are from a flight performed in the following manner:

- Manual take-off (around 50 s in the following plots);
- Switch from flight mode 0 to 1 and then to 2 at 70 s (that corresponds to $\mathcal{L}_1$ speed control);
- Hovering starting at 90 s up to 160 s;
- Lateral speed command;
- Longitudinal speed command: forward, backward, and forward;
- Lateral speed command;
- Longitudinal speed command: forward and backward;
- Flight mode switch from 2 to 1 and then to 0;
- Manual land (around 293 s).

The entire flight is reported and discussed in this section.

The lateral and longitudinal speed reference tracking results are shown in Figures 12 and 13, respectively. In these figures, the flight mode is also displayed. The proposed adaptive control architecture displays good reference tracking on both axes, with a 0 mean error, as shown in the error distributions displayed in Figures 14 and 15. Nevertheless, slight coupling effects on both axes are present during the flight. In particular, for the lateral speed in the interval between $t \approx 200$ s and $t \approx 225$ s, the coupling effects with the longitudinal reference commands are present as for the interval between $t \approx 250$ s

and $t \approx 300$ s. Coupling effects on the longitudinal axis are less evident, but this could also be motivated by the fact that fewer commands were given on the lateral axis in this experiment. Nevertheless, on the longitudinal axis, in the interval from $t \approx 75$ s to $t \approx 95$ s, a clear coupling effect is present due to the commanded lateral reference speed.

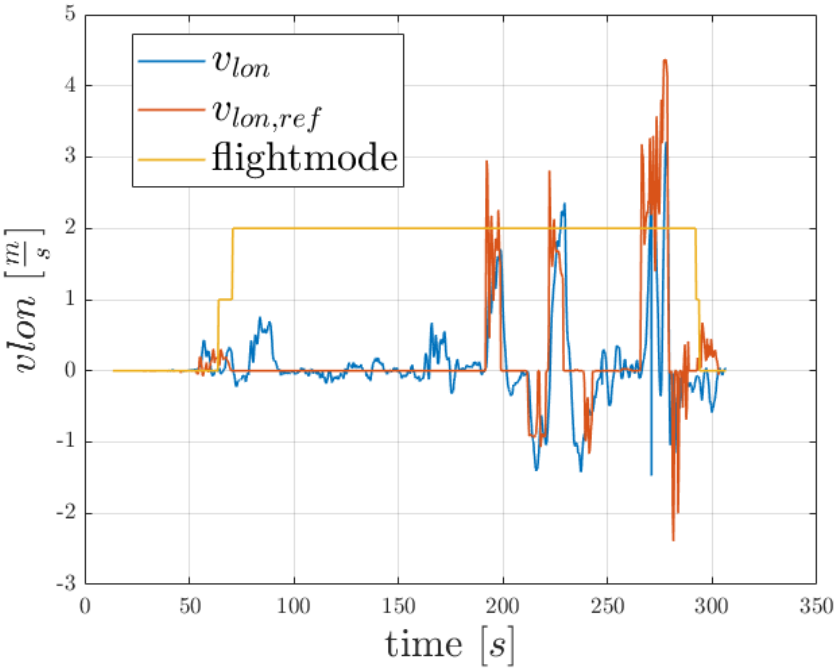

Figure 12. Longitudinal speed reference tracking.

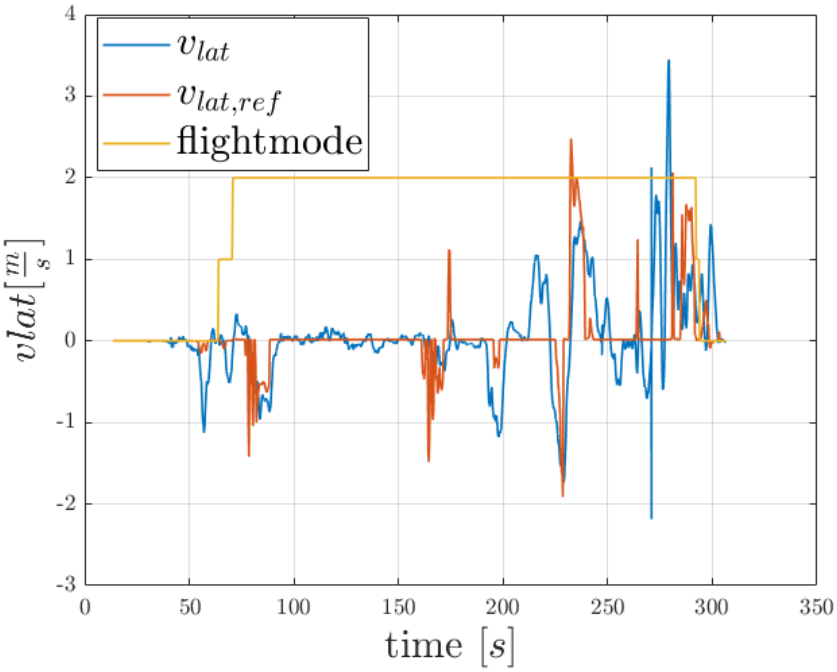

Figure 13. Lateral speed reference tracking.

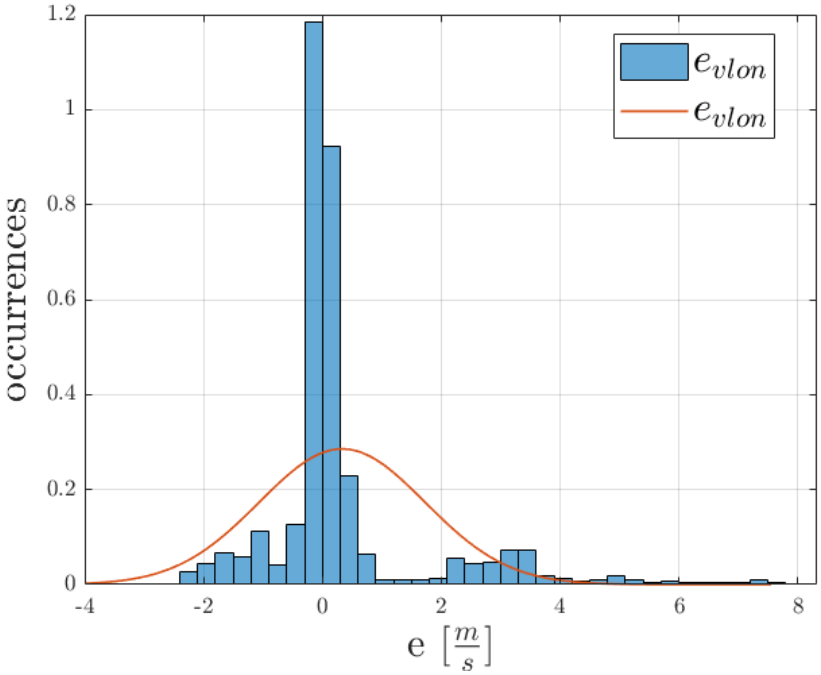

Figure 14. Longitudinal speed tracking error distribution.

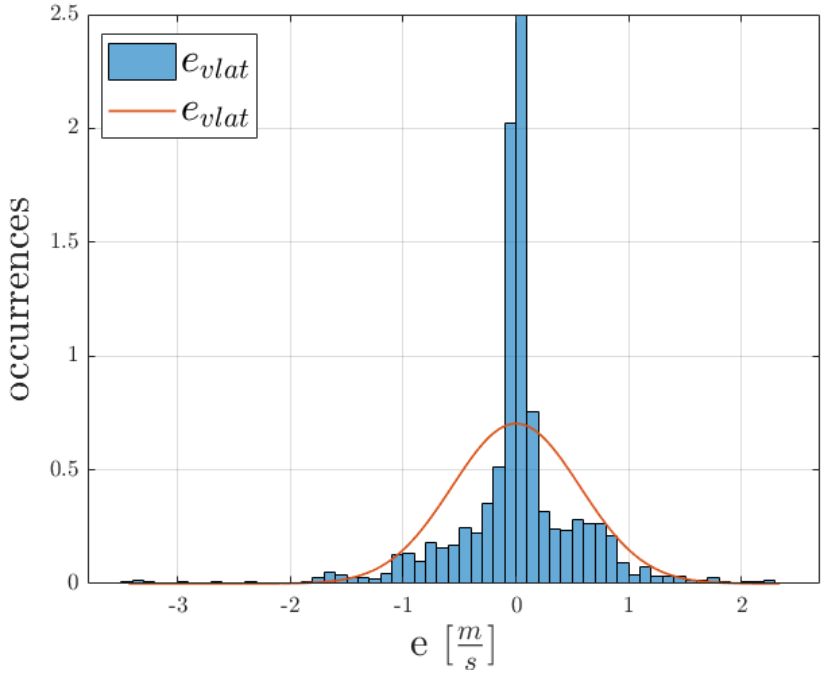

Figure 15. Lateral speed tracking error distribution.

6. Conclusions

In this study, an $\mathcal{L}_1$ algorithm was designed and implemented as a speed autopilot for an unmanned small-scale helicopter. The controller's performance was assessed and compared with a classical PI structure. An extensive numerical simulation campaign demonstrated the adaptive controller's performance in reducing tracking error, compensating model uncertainties, and rejecting external wind disturbances. One of the main contributions of this work is the in-flight testing of the proposed control architecture. The results showed tracking errors comparable to those obtained in simulations. The flight test

campaign validated the proposed solution as a suitable control architecture for small-scale helicopter speed control.

Author Contributions: Conceptualization, A.D.R. and G.B.; methodology, A.D.R. and G.B.; software, G.B. and A.D.R.; validation, G.B. and A.D.R.; formal analysis, G.B. and A.D.R.; investigation, A.D.R., G.B., E.L.d.A., F.G. and L.P.; resources, F.G., E.L.d.A., and L.P.; data curation, G.B. and A.D.R.; writing—original draft preparation, G.B. and A.D.R.; writing—review and editing, F.G., E.L.d.A. and L.P.; visualization, G.B. and A.D.R.; supervision, F.G. and L.P.; project administration, F.G. and E.L.d.A.; funding acquisition, F.G. and E.L.d.A. All authors have read and agreed to the published version of the manuscript.

Funding: This research was founded within the MOST—Sustainable Mobility National Research Center and received funding from the European Union Next-GenerationEU (PIANO NAZIONALE DI RIPRESA E RESILIENZA (PNRR)—MISSIONE 4 COMPONENTE 2, INVESTIMENTO 1.4—D.D. 1033 17/06/2022, CN00000023). This manuscript reflects only the authors' views and opinions, neither the European Union nor the European Commission can be considered responsible for them.

Data Availability Statement: Dataset available upon request from the authors.

Conflicts of Interest: The authors declare no conflicts of interest.

Abbreviations

Symbol	Description	Units
a_0	Rotor coning angle	rad
a_1	Longitudinal TPP deflection angle in rotor–hub system	rad
A_1	Lateral cyclic angle	rad
b_1	Lateral TPP deflection angle in rotor–hub system	rad
B_1	Longitudinal cyclic angle	rad
C_T	Thrust coefficient	
C_M	Pitching moment coefficient	
C_L	Roll moment coefficient	
$C(s)$	Unitary gain low pass filter	
d	Disturbance	
$\boldsymbol{F} = [F_x\ F_y\ F_z]^T$	Force vector	N
$\mathbf{F}$	Reference frame	
g	Gravity acceleration	m/s^2
$G_m(s)$	Reference model transfer function	
$G_p(s)$	Plant transfer function	
$\boldsymbol{I}$	Inertia tensor	kg/m^2
K	Feedforward constant	
K_i	Integral PID gain	
K_p	Proportional PID gain	
$\mathbf{L}_{nl}$	Nonlinear version of the inflow gains matrix	
L	Lipschitz constant	
m	Mass	kg
$\boldsymbol{M} = [M_x\ M_y\ M_z]^T$	Moment vector	Nm
$\mathbf{M}$	Matrix of apparent mass terms	
R_h	Rotor radius	m
s	Complex variable	
t	Time variable	s
$\mathbb{T}$	Rotation matrix	
u	Control input	
$u_{\mathcal{L}_1}$	$\mathcal{L}_1$ input	
$\boldsymbol{V} = [v_{lon}\ v_{lat}\ v_v]^T$	Velocity vector	m/s
w_H	Vertical speed in hub-body frame	m/s
$\mathbf{X}$	Position vector	m
y	Output	
$\hat{y}$	Predictor output	

Greek Symbols		
β	Blade flapping	rad
β_s	Sideslip angle	rad
ϵ	Error signals	
Γ	Adaptive gain	
ϕ, θ, ψ	Roll, pitch, yaw Euler angles	rad
ρ	Density	kg/m^3
λ	Inflow ratio	
λ_0	Uniform inflow ratio	
λ_c	Longitudinal inflow ratio	
λ_s	Lateral inflow ratio	
σ	Adaptive term	
$\hat{\sigma}$	Estimated adaptive term	
θ_{MR}	Blade collective	rad
θ_{TR}	Yaw command	rad
$\mathbf{\Omega} = [p\ q\ r]^T$	Angular velocity vector	rad/s
Ω_h	Rotor angular velocity	rad/s
ζ	Azimuth blade angle	rad
Subscripts Superscripts		
$_{(a)}$	Aerodynamical	
$_b$	Body reference frame	
$_{CG}$	Center of gravity	
$_{des}$	Desired	
$_{(e)}$	External	
$_E$	North–east–down reference frame	
$_{(g)}$	Gravitational	
$_{lat}$	Lateral	
$_{lon}$	Longitudinal	
$_{MR}$	Main rotor	
$_{TR}$	Tail rotor	
Acronyms		
BL	Buttline	
NED	North–east–down	
PID	Proportional–integral–derivative	
RF	Reference frame	
STA	Stationline	
TPP	Tip path plane	
UAV	Unmanned aerial vehicle	
WL	Waterline	

Appendix A

Table A1. UAV helicopter relevant parameters.

Parameter	Symbol	Value	Units
UAV DATA			
Mass	m	4.8	kg
Center of gravity stationline	STA_{CG}	0.34	m
Center of gravity buttline	BL_H	0	m
Center of gravity waterline	WL_H	0.174	m
Moment of inertia	$I_x,\ I_y,\ I_z$	0.0465, 0.2971, 0.2567	kg m^2
Inertia products	$I_{xy},\ I_{yz},\ I_{xz}$	0.0079, 0.0033, 0.0006	kg m^2
MAIN ROTOR (MR)			
Number of blades	N_b	2	-
Radius	R_{MR}	0.79	m
Chord	c_{MR}	0.06	m
Rotational speed	Ω_{MR}	1995.3	rpm

Table A1. *Cont.*

Parameter	Symbol	Value	Units
Hinge offset	ε	0.0314	m
Flapping spring constant	K_β	162.69	N m/rad
Tangent of δ_3	K_1	0	-
Blade twist	θ_{tMR}	0	rad
Precone angle	a_{0MR}	0	rad
Solidity	σ_{MR}	0.0479	-
Lift curve slope	a_{TR}	2*π	1/rad
Blade inertia moment	I_β	0.0344	kg m^2
MR hub stationline	STA_H	0.3305	m
MR hub buttline	BL_H	0	m
MR hub waterline	WL_H	0.35	m
TAIL ROTOR (TR)			
Number of blades	N_b	2	-
Radius	R_{TR}	0.115	m
Chord	c_{TR}	0.031	m
Rotational speed	Ω_{TR}	9976	rpm
Tangent of δ_3	K_{1TR}	0	-
Blade twist	θ_{tMR}	0	rad
Solidity	σ_{TR}	0.1716	-
Lift curve slope	a_{TR}	2*π	1/rad
Blade inertia moment	I_β	0.00002665	kg m^2
TR hub stationline	STA_{TR}	1.385	m
TR hub buttline	BL_{TR}	0.052	m
TR hub waterline	WL_{TR}	0.205	m
FUSELAGE (FUS)			
Fus. aerodynamic ref. point stationline	STA_{FUS}	0	m
Fus. aerodynamic ref. point buttline	BL_{FUS}	0	m
Fus. aerodynamic ref. point waterline	WL_{FUS}	0	m
Frontal area	S_{front}	0.02042	m^2
Lateral area	S_{lat}	0.0633	m^2
Top area	S_{top}	0.09739	m^2

References

1. Manfreda, S.; McCabe, M.F.; Miller, P.E.; Lucas, R.; Madrigal, V.P.; Mallinis, G.; Dor, E.B.; Helman, D.; Estes, L.; Ciraolo, G.; et al. On the Use of Unmanned Aerial Systems for Environmental Monitoring. *Remote Sens.* **2018**, *10*, 641. [CrossRef]
2. Zhang, Z.; Zhu, L. A Review on Unmanned Aerial Vehicle Remote Sensing: Platforms, Sensors, Data Processing Methods, and Applications. *Drones* **2023**, *7*, 398. [CrossRef]
3. Fang, Z.; Savkin, A.V. Strategies for Optimized UAV Surveillance in Various Tasks and Scenarios: A Review. *Drones* **2024**, *8*, 193. [CrossRef]
4. Telli, K.; Kraa, O.; Himeur, Y.; Ouamane, A.; Boumehraz, M.; Atalla, S.; Mansoor, W. A Comprehensive Review of Recent Research Trends on Unmanned Aerial Vehicles (UAVs). *Systems* **2023**, *11*, 400. [CrossRef]
5. Ahmed, F.; Mohanta, J.C.; Keshari, A.; Yadav, P.S. Recent Advances in Unmanned Aerial Vehicles: A Review. *Arab. J. Sci. Eng.* **2022**, *47*, 7963–7984. [CrossRef]
6. Jong, D.; Kang, T.; Dharmayanda, H.; Budiyono, A. H-Infinity Attitude Control System Design for a Small Scale Autonomous Helicopter with Nonlinear Dynamics and Uncertainties. *J. Aerosp. Eng.* **2012**, *25*, 501–518. [CrossRef]
7. Nair, V.V.; Jayasree, P.R.; Parvathy, G. Robust control of helicopter with suspended load. In Proceedings of the 2017 International Conference on Circuit, Power and Computing Technologies (ICCPCT), Kollam, India, 20–21 April 2017; pp. 1–6. [CrossRef]
8. Raptis, I.A.; Valavanis, K.P. Linear and Nonlinear Control of Small-Scale Unmanned Helicopters. In *Intelligent Systems, Control and Automation: Science and Engineering*; Springer: Dordrecht, The Netherlands, 2011; Volume 45. [CrossRef]
9. Zhao, W.; Meng, Z.; Wang, K.; Zhang, H. Backstepping control of an unmanned helicopter subjected to external disturbance and model uncertainty. *Appl. Sci.* **2021**, *11*, 5331. [CrossRef]
10. Wan, M.; Chen, M.; Lungu, M. Integral Backstepping Sliding Mode Control for Unmanned Autonomous Helicopters Based on Neural Networks. *Drones* **2023**, *7*, 154. [CrossRef]
11. Xian, B.; Jianchuan, G.; Yao, Z.; Bo, Z. Sliding mode tracking control for miniature unmanned helicopters. *Chin. J. Aeronaut.* **2015**, *28*, 277–284. [CrossRef]

12. Halbe, O.; Hajek, M. Robust helicopter sliding mode control for enhanced handling and trajectory following. *J. Guid. Control. Dyn.* **2020**, *43*, 1805–1821. [CrossRef]
13. Liceaga-Castro, E.; Bradley, R.; Castro-Linares, R. Helicopter control design using feedback linearization techniques. In Proceedings of the 28th IEEE Conference on Decision and Control, Tampa, FL, USA, 13–15 December 1989; Volume 1, pp. 533–534. [CrossRef]
14. Nidya, M.V.; Mija, S.J.; Jacob, J. Feedback-linearization based robust relatively optimal trajectory tracking controller for 3-DOF helicopter. *Eng. Sci. Technol. Int. J.* **2022**, *31*, 101050. [CrossRef]
15. Mohammadzahri, M.; Khaleghifar, A.; Ghodsi, M.; Soltani, P.; AlSulti, S. A discrete approach to feedback linearization, yaw control of an unmanned helicopter. *Unmanned Syst.* **2023**, *11*, 57–66. [CrossRef]
16. Pavel, M.; Shanthakumaran, P.; Chu, Q.; Stroosma, O.; Wolfe, M.; Cazemier, H. Incremental nonlinear dynamic inversion for the Apache AH-64 helicopter control. *J. Am. Helicopter Soc.* **2020**, *65*. [CrossRef]
17. Zhang, S.; Zhang, H.; Ji, K. Incremental nonlinear dynamic inversion attitude control for helicopter with actuator delay and saturation. *Aerospace* **2023**, *10*, 521. [CrossRef]
18. Liu, C.; Chen, W.H.; Andrews, J. Model predictive control for autonomous helicopters with computational delay. In Proceedings of the UKACC International Conference on Control, Coventry, UK, 7–10 September 2010; pp. 1–6. [CrossRef]
19. Joelianto, E.; Sumarjono, E.; Budiyono, A.; Penggalih, D. Model predictive control for autonomous unmanned helicopters. *Aircr. Eng. Aerosp. Technol. Int. J.* **2011**, *83*, 375–387. [CrossRef]
20. Greer, W.B.; Sultan, C. Infinite horizon model predictive control tracking application to helicopters. *Aerosp. Sci. Technol.* **2020**, *98*, 105675. [CrossRef]
21. Chikasha, P.N.; Dube, C. Adaptive model predictive control for a quadrotor. *IFAC-PapersOnLine* **2017**, *50*, 157–162. [CrossRef]
22. Dutta, L.; Das, D. Adaptive model predictive control design using multiple model second level adaptation for parameter estimation of two-degree freedom of helicopter model. *Int. J. Robust Nonlinear Control* **2021**, *31*, 3248–3278. [CrossRef]
23. Wang, Y.; Li, A.; Yang, S.; Li, Q.; Ma, Z. A neural network based MRAC scheme with application to an autonomous nonlinear rotorcraft in the presence of input saturation. *ISA Trans.* **2021**, *115*, 1–11. [CrossRef]
24. Wang, Y.; Li, A.; Yang, S.; Tian, H. A model reference adaptive control scheme of a high-order nonlinear helicopter subject to input and state constraints. *J. Frankl. Inst.* **2022**, *359*, 6709–6734. [CrossRef]
25. Sadeghzadeh, I.; Mehta, A.; Zhang, Y. Fault tolerant control of a quadrotor helicopter using model reference adaptive control. In Proceedings of the International Design Engineering Technical Conferences and Computers and Information in Engineering Conference, Washington, DC, USA, 28–31 August 2011; Volume 54808, pp. 997–1004.
26. Xu, W.; Zhang, F.; Lin, D. System identification and adaptive control of micro helicopter. In *Journal of Physics: Conference Series*; IOP Publishing: Bristol, UK, 2021; Volume 1780, p. 012026.
27. Subramanian, R.G.; Elumalai, V.K. Robust MRAC augmented baseline LQR for tracking control of 2 DoF helicopter. *Robot. Auton. Syst.* **2016**, *86*, 70–77. [CrossRef]
28. Cao, C.; Hovakimyan, N. Design and analysis of a novel l1 adaptive controller, part I: Control signal and asymptotic stability. In Proceedings of the 2006 American Control Conference, Minneapolis, MN, USA, 14–16 June 2006; IEEE: Piscataway, NJ, USA, 2006; pp. 3397–3402.
29. Cao, C.; Hovakimyan, N. Stability margins of $\mathcal{L}_1$ adaptive controller: Part ii. In Proceedings of the American Control Conference, New York, NY, USA, 9–13 July 2007.
30. Cao, C.; Hovakimyan, N. $\mathcal{L}_1$ adaptive controller for systems with unknown time-varying parameters and disturbances in the presence of non-zero trajectory initialization error. *Int. J. Control* **2008**, *81*, 1148–1162. [CrossRef]
31. Cao, C.; Hovakimyan, N. Design and analysis of a novel $\mathcal{L}_1$ adaptive control architecture with guaranteed transient performance. *IEEE Trans. Autom. Control* **2008**, *53*, 586–591. [CrossRef]
32. Cao, C.; Hovakimyan, N. $\mathcal{L}_1$ adaptive output feedback controller for systems of unknown dimension. *IEEE Trans. Autom. Control* **2008**, *53*, 815–821. [CrossRef]
33. Wnag, J.; Vijay, V.P.; Cao, C.; Hovakimyan, N.; Lavretsky, E. Novel L1 adaptive control methodology for aerial refueling with guaranteed transient performance. *J. Guid. Control. Dyn.* **2008**, *31*, 182–193. [CrossRef]
34. Gregory, I.; Cao, C.; Xargay, E.; Hovakimyan, N.; Zou, X. L1 adaptive control design for NASA AirSTAR flight test vehicle. In Proceedings of the AIAA Guidance, Navigation, and Control Conference, Chicago, IL, USA, 10–13 August 2009. [CrossRef]
35. Hellmundt, F.; Wildschek, A.; Maier, R.; Osterhuber, R.; Holzapfel, F. Comparison of L1 Adaptive Augmentation Strategies for a Differential PI Baseline Controller on a Longitudinal F16 Aircraft Model. In *Advances in Aerospace Guidance, Navigation and Control*; Springer: Cham, Switzerland, 2018; pp. 99–118. [CrossRef]
36. Bichlmeier, M.; Holzapfel, F.; Xargay, E.; Hovakimyan, N. $\mathcal{L}_1$ Adaptive Augmentation of a Helicopter Baseline Controller. In Proceedings of the AIAA Guidance, Navigation, and Control (GNC) Conference, Boston, MA, USA, 19–22 August 2013.
37. Song, T.; Wang, J.; Lin, D.; Pei, P. $\mathcal{L}_1$ adaptive control design of a helicopter in vertical flight. *Proc. Inst. Mech. Eng. Part J. Aerosp. Eng.* **2020**, *234*, 2089–2099.
38. Guerreiro, B.J.; Silvestre, C.; Cunha, R.; Cao, C.; Hovakimyan, N. L1 adaptive control for autonomous rotorcraft. In *American Control Conference*; IEEE: Piscataway, NJ, USA, 2009; pp. 3250–3255.

39. Ryals, A.D.; Bertolani, G.; Pollini, L.; Giulietti, F. L1 adaptive attitude augmentation of a small scale unmanned helicopter. In Proceedings of the 2023 International Conference on Unmanned Aircraft Systems (ICUAS), Warsaw, Poland, 6–9 June 2023; pp. 1081–1088. [CrossRef]
40. Bertolani, G.; Ryals, A.D.; Pollini, L.; Giulietti, F. L1 adaptive speed control for a helicopter. In Proceedings of the 48th European Rotorcraft Forum, ERF 2022, Winterthur, Switzerland, 6–8 September 2022.
41. Harada, M.; Ichikawa, R.; Watanabe, S.; Bollino, K. L_1 Adaptive Control for a Single Coaxial Rotor MAV. In Proceedings of the AIAA Guidance, Navigation, and Control Conference, San Diego, CA, USA, 4–8 January 2016; American Institute of Aeronautics and Astronautics: Reston, VA, USA. [CrossRef]
42. Szafranski, G.; Roman, C. Different approaches of PID control UAV type quadrotor. In Proceedings of the International Micro Air Vehicles Conference, Harde, The Netherlands, 12–15 September 2011; pp. 70–75.
43. Lavretsky, E.; Gibson, T.E. Projection Operator in Adaptive Systems. *arXiv* **2012**, arXiv:1112.4232.
44. Mettler, B. *Identification Modeling and Characteristics of Miniature Rotorcraft*; Springer: Cham, Switzerland, 2002.
45. Talbot, P.D.; Tinling, B.E.; Decker, W.A.; Chen, R.T.N. *A mathematical Model for a Single Main Rotor Helicopter for Piloted Simulation*; Ames Reasearch Center Moffett: Field, CA, USA, 1982
46. Heffley, R.; Mnich, M.A. *Minimum Complexity Helicopter Simulation Math Model*. Ames Research Center: Mountain View, CA, USA, 1988.
47. Peters, D.A.; HaQuang, N. Dynamic inflow for practical applications. *J. Am. Helicopter Soc.* **1988**, *33*, 64–68. [CrossRef]
48. *NOAA-S/T 76-1562*; U.S. Standard Atmosphere. U.S. Government Printing Office: Washington, DC, USA, 1976.
49. Leishman, J.G. *Principles of Helicopter Aerodynamics*; Cambridge aerospace series 12; Cambridge University Press: Cambridge, UK, 2000.
50. Dormand, J.; Prince, P. A family of embedded Runge-Kutta formulae. *J. Comput. Appl. Math.* **1980**, *6*, 19–26. [CrossRef]
51. U.S. Military Specification MIL-F-8785C. 1980. Available online: http://www2.coe.pku.edu.cn/tpic/2011971042474.pdf (accessed on 1 July 2024).
52. U.S. Military Handbook MIL-HDBK-1797B. 2012. Available online: https://www.abbottaerospace.com/downloads/mil-hdbk-1797-department-of-defense-interface-standard-flying-qualities-of-piloted-aircraft/ (accessed on 1 July 2024).
53. Pixhawk Website. Available online: https://pixhawk.org/ (accessed on 1 July 2024).
54. UAV Toolbox Support Package for PX4 Autipilots Website. Available online: https://www.mathworks.com/help/uav/px4-spkg.html (accessed on 1 July 2024).